

The Impact of $^{12}\text{C}(\alpha, \gamma)^{16}\text{O}$ Reaction on the Evolution of He Stars

Gang Long^{1,2,3}, Yu Wang^{1,2,3}, Dongdong Liu^{1,2,3}, Jianguo Wang^{1,2,3} and Bo Wang^{1,2,3}

¹ Yunnan Observatories, Chinese Academy of Sciences, Kunming 650216, China;

liudongdong@ynao.ac.cn; wangjg@ynao.ac.cn; wangbo@ynao.ac.cn

² International Centre of Supernovae, Yunnan Key Laboratory, Kunming 650216, China

³ University of Chinese Academy of Sciences, Beijing 100049, China

Received 20xx month day; accepted 20xx month day

Abstract The $^{12}\text{C}(\alpha, \gamma)^{16}\text{O}$ reaction is one of the most important reactions in the evolution of massive stars, yet its rate is still highly uncertain. In this work, we investigated how variations in the $^{12}\text{C}(\alpha, \gamma)^{16}\text{O}$ reaction rate affect the evolution of a $14 M_{\odot}$ He star using the MESA code. Our simulations indicate that the $^{12}\text{C}(\alpha, \gamma)^{16}\text{O}$ reaction rate determines the conditions for C burning, affecting its explodability. As the reaction rate increases, central C-burning becomes neutrino-dominated, transitioning from the convective to the radiative regime. This leads to higher compactness and a larger iron core, indicating a more compact pre-SN core structure that is difficult to explode. Conversely, lower reaction rates shorten the C-burning lifetime and trigger earlier central Ne ignition, which counteracts core contraction. This results in reduced compactness and iron core mass. We also found that variations in reaction rates shift the location of the last C-burning shell. When this shell exceeds the mass coordinate used for compactness evaluation, the overall compactness increases significantly. Although the Si- and O-burning convective shells decrease compactness, the overall increase remains unaffected. This work suggests that the $^{12}\text{C}(\alpha, \gamma)^{16}\text{O}$ reaction play an important role in the pre-SN core structure and potentially impact the explodability of massive He stars.

Key words: stars: massive — stars: evolution — stars: abundances — stars: black holes

1 INTRODUCTION

Massive He stars are thought to be stripped products of more massive stars that have lost their hydrogen-rich envelopes through stellar winds or binary interactions (e.g. Podsiadlowski et al. 1992; Pols & Dewi 2002; Crowther 2007; Langer 2012; Yoon 2017; Dessart et al. 2020). These stars end their lives as core-collapse supernovae (CCSNe), leaving behind neutron stars (NSs) or black holes (BHs)(e.g. Woosley 2019; Ertl et al. 2020). Their final fates are mainly determined by the carbon-oxygen (CO) core mass M_{CO} and the central carbon mass fraction $X_{\text{i}}(^{12}\text{C})$ at the end of core He burning, both of which are sensitive to the

$^{12}\text{C}(\alpha, \gamma)^{16}\text{O}$ reaction (Weaver & Woosley 1993; Woosley & Heger 2007; Tur et al. 2007, 2010; Chieffi & Limongi 2020; Patton & Sukhbold 2020; Sukhbold & Adams 2020; Farmer et al. 2020; Schneider et al. 2021, 2023; Laplace et al. 2025). However, its reaction rate remains highly uncertain (deBoer et al. 2017). Therefore, it is important to investigate the influence of the uncertainty in the $^{12}\text{C}(\alpha, \gamma)^{16}\text{O}$ reaction rate on the evolution and the pre-supernova (pre-SN) core structure.

The $^{12}\text{C}(\alpha, \gamma)^{16}\text{O}$ reaction is one of the most important reactions in the evolution of massive stars (Weaver & Woosley 1993; Woosley et al. 2003). Its rate determines the ratio of ^{12}C and ^{16}O after He burning by competing with the well-determined triple-alpha (3α) reaction (Buchmann 1996; Imbriani et al. 2001; Kunz et al. 2002; Woosley et al. 2003; El Eid et al. 2004; Tur et al. 2007; Woosley & Heger 2007; Austin et al. 2014). Variations in these abundances have significant effects on subsequent burning stages, as well as the core structure and nucleosynthesis (Imbriani et al. 2001; Tur et al. 2007, 2010; West et al. 2013; Farmer et al. 2020). For instance, Imbriani et al. (2001) investigated how variations in the $^{12}\text{C}(\alpha, \gamma)^{16}\text{O}$ reaction impact the residual ^{12}C mass fraction after helium burning, which determines whether C burning proceeds radiatively or convectively, thereby affecting the pre-SN core structure and the explodability of stars (Sukhbold & Woosley 2014; Sukhbold et al. 2016; Sukhbold & Adams 2020; Patton & Sukhbold 2020; Schneider et al. 2021). Additionally, several studies have explored the impact of uncertainties in this reaction on nucleosynthesis (Weaver & Woosley 1993; Tur et al. 2010; Farmer et al. 2023). Notably, uncertainties in this reaction rate also affect the ranges of both the pair-instability (PI) mass gap and the BH mass gap (Farmer et al. 2019, 2020; Costa et al. 2021; Woosley & Heger 2021). Motivated by these studies, we focus on the impact of the $^{12}\text{C}(\alpha, \gamma)^{16}\text{O}$ reaction rate on the pre-SN core structure and the explodability of the star.

Previous studies investigated the connection between the final pre-SN structure and the outcome of neutrino-driven CCSN explosions, aiming to predict the explodability of progenitors, i.e., whether the progenitors will explode as a SN or not (e.g. O’Connor & Ott 2011; Ugliano et al. 2012; Ertl et al. 2016; Müller et al. 2016). O’Connor & Ott (2011) proposed the compactness parameter $\xi_{2.5}$ to characterize the core structure and proposed it as a criterion to assess stellar explodability. Progenitors with higher compactness are more difficult to explode (e.g. O’Connor & Ott 2011; Ugliano et al. 2012; Sukhbold & Woosley 2014; Müller et al. 2016; Sukhbold et al. 2016; Sukhbold & Adams 2020; Chieffi & Limongi 2020). Additionally, a two-parameter criterion related to the density and entropy at the Si/O interface was used to distinguish between successful and failed explosions (Ertl et al. 2016, 2020). Thus, we use these parameters to characterize the final core structure and explore the explodability of progenitors.

In this work, we aim to investigate the impact of uncertainties in the $^{12}\text{C}(\alpha, \gamma)^{16}\text{O}$ reaction rate on the evolution of massive He stars and predict their final fates. The paper is organized as follows. In Section 2, we describe the basic assumptions and numerical methods. The simulation results are presented in Section 3. Finally, we discuss our results in Section 4, and conclude in Section 5.

2 METHOD

To investigate the impact of the $^{12}\text{C}(\alpha, \gamma)^{16}\text{O}$ reaction rate on the core structure of massive He stars, we use the MESA code (version 10398; Paxton et al. 2011, 2013, 2015, 2018, 2019) to simulate the evolution

of the 14 M_\odot He star models with different $^{12}\text{C}(\alpha, \gamma)^{16}\text{O}$ reaction rates, from the He zero-age main sequence (He-ZAMS) to the onset of core collapse, defined as when the contraction velocity in the iron core boundary reaches 1000 km s^{-1} . The initial He star models are constructed with a metallicity of $Z = 0.02$ (see also Aguilera-Dena et al. 2022), and we adopt the wind mass-loss prescription from Yoon (2017). For the $^{12}\text{C}(\alpha, \gamma)^{16}\text{O}$ reaction rates, we use MESA's default rates from Angulo et al. (1999, hereafter NACRE), and also consider two widely used compilations from Caughlan & Fowler (1988, hereafter CF88) and Kunz et al. (2002, hereafter Kunz), both of which report lower reaction rates compared to the MESA default. Convection is treated using the standard mixing-length theory (Böhm-Vitense 1958), with a mixing-length parameter of $\alpha_{\text{MLT}} = 2.0$, and convective boundaries are determined using the Ledoux criterion. We apply exponential overshooting with a parameter of $f_{\text{ov}} = 0.016$ during core He burning (Herwig 2000). Additionally, we adopt a semiconvection efficiency parameter of $\alpha_{\text{SEM}} = 1.0$, and a thermohaline diffusion coefficient of $D_{\text{TH}} = 1.0$.

To evaluate the explodability of progenitors, we focus on the compactness criterion and the two-parameter criterion, due to their widespread use in predicting whether iron core collapse will result in a successful or failed neutrino-driven SN mechanism. The compactness parameter $\xi_{2.5}$ characterizes the core structure and is defined as (O'Connor & Ott 2011)

$$\xi_M \equiv \frac{M/\text{M}_\odot}{R(M)/1000 \text{ km}}, \quad (1)$$

where M and $R(M)$ are the enclosed mass and the radius as a function of the mass coordinate, respectively. The typical mass used to evaluate explodability is $M = 2.5 \text{ M}_\odot$. The parameter $\xi_{2.5}$ is closely related to the iron core mass, with both quantities commonly used to characterize the final core structure (e.g. Brown et al. 2001; O'Connor & Ott 2011; Sukhbold & Woosley 2014; Ertl et al. 2016; Müller et al. 2016; Patton & Sukhbold 2020; Laplace et al. 2025). The two-parameter criterion consists of M_4 and μ_4 proposed by Ertl et al. (2016):

$$\mu_4 \equiv \frac{dm/\text{M}_\odot}{dr/1000 \text{ km}} \Big|_{s=4}. \quad (2)$$

Here, M_4 and μ_4 represent the mass and radial coordinates where the entropy per baryon reaches 4.0 k_B , and they are related to the density and entropy distributions. Meanwhile, μ_4 and $\mu_4 \times M_4$ are indirectly related to the mass accretion rate at the time of explosion and the accretion luminosity, respectively. Based on this, the likely explosion and collapse models are distinguished by the relation $\mu_4 = 0.294\mu_4 M_4 + 0.0468$ from Ertl et al. (2020). Additionally, we use the semianalytic approach of Müller et al. (2016), which is based on the neutrino-driven CCSN explosions, to predict whether stars explode as SNe or collapse into BHs obtain the properties of successful SN explosion, such as explosion energy E_{exp} and gravitational remnant mass $M_{\text{rm,grav}}$.

3 PRE-SN EVOLUTION AND CORE STRUCTURE

In this section, we examine the impact of the uncertainty in the $^{12}\text{C}(\alpha, \gamma)^{16}\text{O}$ reaction rate on the evolution of massive He stars, particularly their chemical composition and core structure. As ^4He is depleted and ^{12}C accumulates during core He burning, the $^{12}\text{C}(\alpha, \gamma)^{16}\text{O}$ reaction becomes dominant and strongly affects the subsequent evolution. To further illustrate this, we explore its effect on the mass fractions of ^{12}C and the CO

Table 1: Pre-SN Properties with Varying $^{12}\text{C}(\alpha, \gamma)^{16}\text{O}$ Reaction Rates

Rate	M_{CO}	$X_{\text{i}}(^{12}\text{C})$	$X_{\text{i}}(^{16}\text{O})$	$M_{\text{C-free}}$	$\xi_{2.5}$	μ_4	M_4	s_{c}	M_{f}	M_{Fe}	$\log(-E_{\text{bind}})$	E_{exp}	Fate	$M_{\text{rm,grav}}$
	[M_{\odot}]			[M_{\odot}]				[$N_{\text{A}} k_{\text{B}}$]	[M_{\odot}]	[M_{\odot}]	[erg]	[10^{51}erg]		[M_{\odot}]
NACRE	7.12	0.260	0.713	2.73	0.44	0.13	2.15	1.06	8.29	1.79	51.61	...	BH	8.29
CF88	7.18	0.286	0.687	2.06	0.16	0.07	1.77	0.92	8.34	1.54	51.40	0.57	NS	1.55
Kunz	7.21	0.298	0.675	1.75	0.08	0.03	1.52	0.79	8.36	1.46	51.22	0.23	NS	1.34

Notes: The table summarizes key pre-SN properties for the $14 M_{\odot}$ He star with varying $^{12}\text{C}(\alpha, \gamma)^{16}\text{O}$ reaction rates. Three sets of reaction rates from NACRE (Angulo et al. 1999), CF88 (Caughlan & Fowler 1988), and Kunz (Kunz et al. 2002) were employed, with the rates decreasing sequentially. The following quantities are provided: the CO core mass M_{CO} , the central ^{12}C mass fraction $X_{\text{i}}(^{12}\text{C})$, and the central ^{16}O mass fraction $X_{\text{i}}(^{16}\text{O})$, all measured at the end of core He burning when the central helium abundance drops below 10^{-4} ; the C-free core mass $M_{\text{C-free}}$, defined as the mass coordinate where the $X_{\text{i}}(^{12}\text{C})$ falls below 10^{-5} ; the compactness parameter $\xi_{2.5}$; the central specific entropy at core collapse s_{c} ; the radial mass derivative μ_4 and enclosed mass M_4 at a specific entropy of $s = 4$; the final mass M_{f} ; the iron core mass at core collapse M_{Fe} ; the gravitational binding energy of the material above the iron core $-E_{\text{bind}}$; the explosion energy E_{exp} ; the predicted final fate; and the gravitational remnant mass $M_{\text{rm,grav}}$. Both E_{exp} and $M_{\text{rm,grav}}$ are computed following the semi-analytic approach of Müller et al. (2016).

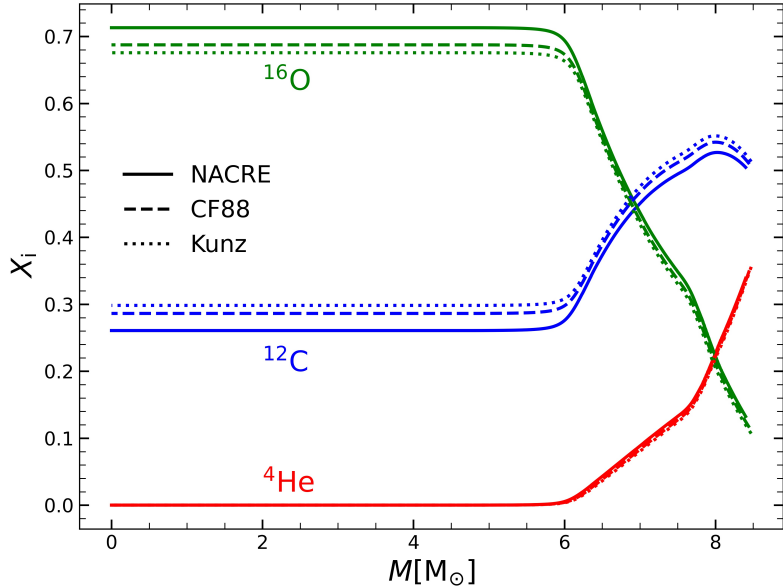


Fig. 1: Profiles of abundance of ^{4}He , ^{12}C , and ^{16}O at the end of core He burning for $14 M_{\odot}$ He stars, calculated using different reaction rates. The solid, dashed, and dotted lines correspond to reaction rates from NACRE, CF88, and Kunz, respectively. The red, blue, and green lines represent the abundances of ^{4}He , ^{12}C , and ^{16}O , respectively.

core mass during core He burning, as well as their influence on subsequent carbon and advanced burning phases, particularly the evolution of compactness and core structure.

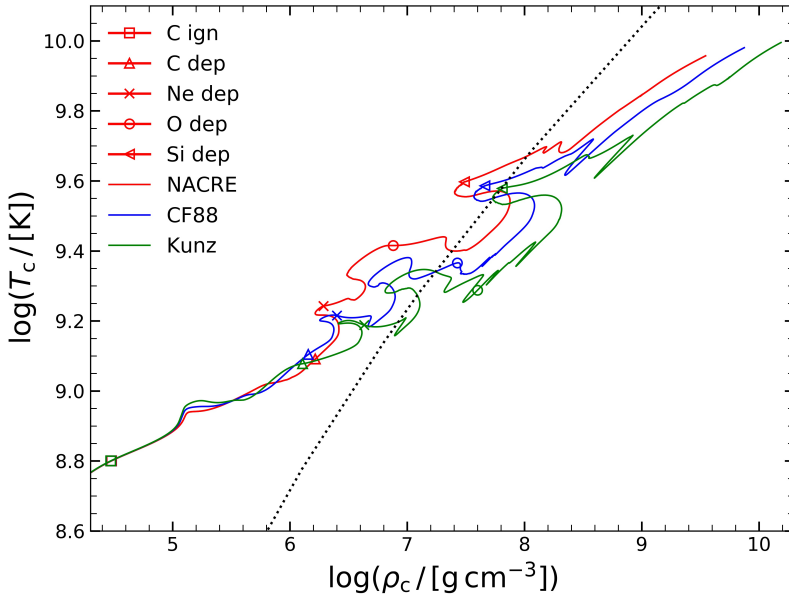


Fig. 2: The evolution of the central temperature T_c as a function of central density ρ_c for the $14 M_\odot$ He stars with three different $^{12}\text{C}(\alpha, \gamma)^{16}\text{O}$ reaction rates (see Table 1), with each reaction rate represented by a different colored curve. Key evolutionary phases are indicated by the following symbols: pentagon for central He depletion, square for central C ignition at $T_c = 8 \times 10^8$ K, triangle for central C depletion, cross for central Ne depletion, open circle for central O depletion, and left-pointing triangle for central Si depletion. The depletion of these elements is defined as the stage when their central mass fraction X_i falls below 10^{-4} . The gray dotted line marks the boundary between non-degenerate and degenerate electron gas.

3.1 Core composition after core helium burning

Varying the $^{12}\text{C}(\alpha, \gamma)^{16}\text{O}$ reaction rate affects the chemical composition of the core. Specifically, a higher reaction rate results in less ^{12}C and more ^{16}O at the end of core He burning, while a lower reaction rate leads to the opposite due to fewer α captures by ^{12}C (deBoer et al. 2017). Fig. 1 shows the abundance profiles of ^4He , ^{12}C , and ^{16}O at the end of core He burning for a $14 M_\odot$ He star, under the various reaction rate scenarios considered. Notably, because the Kunz reaction rate is lower than both the NACRE and CF88 rates, it results in a higher $X_i(^{12}\text{C})$ and a lower $X_i(^{16}\text{O})$ (see also Table 1). For instance, we obtain $X_i(^{12}\text{C}) \approx 0.260$, $X_i(^{12}\text{C}) \approx 0.286$, and $X_i(^{12}\text{C}) \approx 0.298$ for using NACRE, CF88, and Kunz reaction rates, respectively. However, despite these differences in chemical composition, we find that the M_{CO} at the end of core He burning is insensitive to variations in the $^{12}\text{C}(\alpha, \gamma)^{16}\text{O}$ reaction rates. For the models using the NACRE, CF88, and Kunz rates, the values of M_{CO} are $7.12 M_\odot$, $7.18 M_\odot$, and $7.21 M_\odot$, respectively. The small change in the CO core mass is expected, as it is primarily determined by the convective core mass during core He burning, which is mainly influenced by the total energy from the 3α and $^{12}\text{C}(\alpha, \gamma)^{16}\text{O}$ reactions. Since the latter contributes relatively little to energy generation, the 3α process dominates (Woosley et al. 2002).

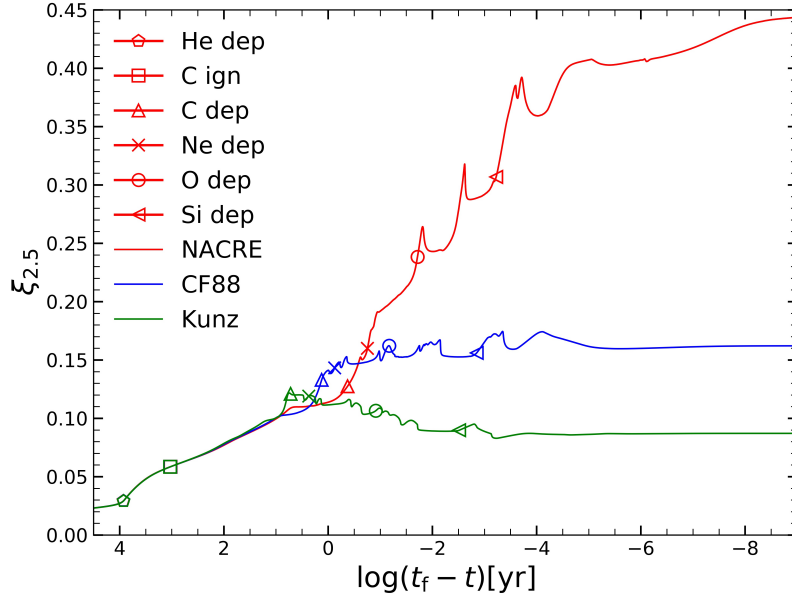


Fig. 3: Time evolution of the compactness parameter $\xi_{2.5}$ for three different $^{12}\text{C}(\alpha, \gamma)^{16}\text{O}$ reaction rate models, from He-ZAMS to the onset of core collapse. Key evolutionary phases are marked by symbols, as described in Fig. 2

3.2 Carbon burning phase

As shown in Sec. 3.1, the $^{12}\text{C}(\alpha, \gamma)^{16}\text{O}$ reaction affects both M_{CO} and $X_i(^{12}\text{C})$. Even small variations in these quantities can have a significant impact on the subsequent core structure and the final fate (Sukhbold & Woosley 2014; Sukhbold & Adams 2020; Patton & Sukhbold 2020; Chieffi & Limongi 2020). Fig. 2 illustrates the evolutionary tracks of central density and temperature after central He depletion, with each curve corresponding to a different adopted reaction rate, revealing notable differences. These differences are driven by the energy generation rate from C burning, $\epsilon_n \sim X_i(^{12}\text{C})^2 \rho T^{23}$, and the energy loss rate through neutrinos, $\epsilon_v \sim T^{12} \rho^{-1}$, where ρ and T represent the density and temperature near the centre (Sukhbold & Adams 2020). Both ϵ_n and ϵ_v depend on ρ and T , which are governed by M_{CO} and $X_i(^{12}\text{C})$. For example, during core C burning, the NACRE model results in lower temperatures at a given central density compared to the CF88 and Kunz models, but it shows an overall shift toward higher central temperatures after carbon depletion.

The differences in the core structure are also reflected in the evolution of the compactness parameter. Fig. 3 shows the evolution of $\xi_{2.5}$ for three different $^{12}\text{C}(\alpha, \gamma)^{16}\text{O}$ reaction rates in $14 M_{\odot}$ He stars from He-ZAMS to the onset of core collapse. During the core He burning, the $\xi_{2.5}$ of all models increases at the same rate, due to the overall contraction of the core, with energy primarily dominated by the 3α reaction. Following core He depletion, the core continues to contract until central C ignition is reached. However, after central C ignition, the evolution of $\xi_{2.5}$ in all models begins to diverge, showing significant differences. This divergence is primarily due to the nature of central C burning, the complex interactions between various convective shells, and the influence of electron degeneracy pressure (Brown et al. 2001;

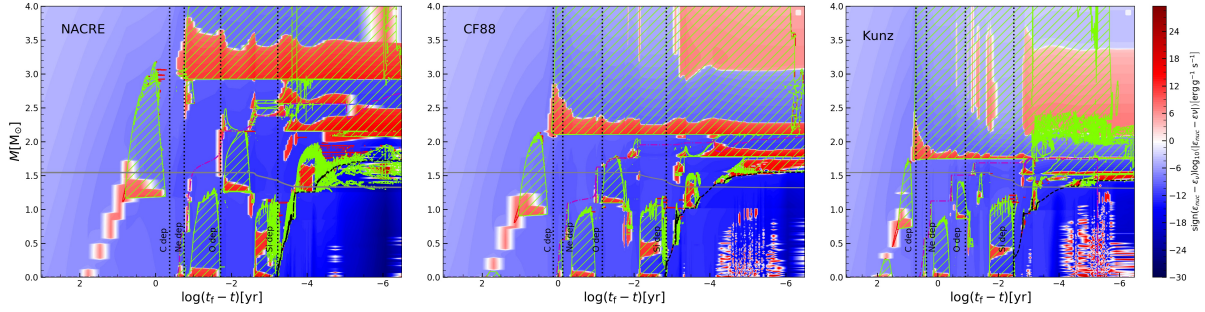


Fig. 4: Kippenhahn diagram for a $14 M_{\odot}$ He stars based on different $^{12}\text{C}(\alpha, \gamma)^{16}\text{O}$ reaction rates (NACRE, CF88 and Kunz), from He-ZAMS to the onset of core collapse. The color bar represents the nuclear energy generation rate ϵ_{nuc} (red) and the neutrino loss rate ϵ_{ν} (blue) gradients. The green and red-hatched regions correspond to the convective and semiconvective mixing regions, respectively. The grey solid line represents the classical Chandrasekhar mass $M_{\text{Ch},0}$, as defined by Timmes et al. (1996). The burning front is defined as the mass coordinate at which the peak energy generation rate occurs for a specific nuclear burning process, such as the base of the convective burning zone. The magenta dash-dotted line represents the C-free core mass $M_{\text{C-free}}$. The black dashed line marks the iron core mass, while the dotted lines, from left to right, represent the depletion of central C, Ne, O, and Si.

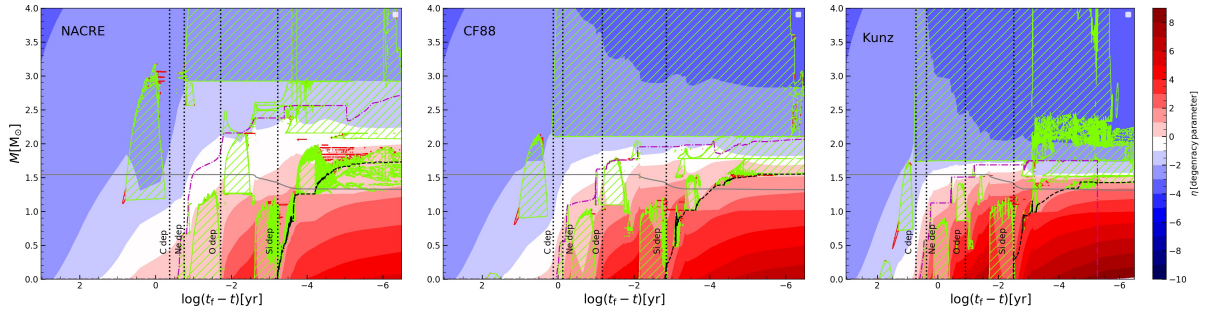


Fig. 5: Same as Fig. 4, but the color bar represents the dimensionless electron degeneracy parameter, $\eta \equiv \mu/k_B T$, where μ is the chemical potential, k_B is the Boltzmann constant, and T is the temperature. For $\eta \ll -1$: non-degenerate; $\eta \approx 0$: partially degenerate; $\eta \gg 1$: strongly degenerate.

Sukhbold & Woosley 2014; Renzo et al. 2017; Chieffi & Limongi 2020; Sukhbold & Adams 2020; Patton & Sukhbold 2020; Laplace et al. 2025).

Fig. 4 shows the Kippenhahn diagrams of the inner $4.0 M_{\odot}$ core structure from C ignition to core collapse for models with different $^{12}\text{C}(\alpha, \gamma)^{16}\text{O}$ reaction rates. In models with different $^{12}\text{C}(\alpha, \gamma)^{16}\text{O}$ reaction rates, lower reaction rates lead to higher $X_i(^{12}\text{C})$, setting the initial conditions for core C burning. As $X_i(^{12}\text{C})$ increases, the nuclear energy generation rate ϵ_n exceeds the neutrino energy loss rate ϵ_v , triggering the transition of central C-burning from radiative to convective, accompanied by variations in the location and strength of the convective C-burning shells. For instance, in the model using the NACRE rate (see the left panel of Fig. 4), central C-burning forms radiatively. After its exhaustion, the significant decline in ϵ_n induces core contraction, which in turn triggers self-regulation of the core structure. This mechanism drives the rapid expansion and cooling of the outer layers, forming the first C-burning convective shell, followed by the second C-burning convective shell. Thus, the location of the burning front, which reflects the ex-

tent of core contraction below, corresponds to a mass coordinate of $M_r \approx 1.16 M_\odot$ for the first C-burning convective shell. In contrast, the models using the CF88 and Kunz reaction rates (see the middle and right panels of Fig. 4), a small convective C-burning core develops, along with two gradually contracting convective C-burning shells. In these models, The mass coordinates of the burning fronts for the first C-burning convective shell are approximately $0.90 M_\odot$ and $0.71 M_\odot$, respectively. These values are lower than the mass coordinates of the burning front in the NACRE model, indicating that the core is more expanded during this phase. As shown in Fig. 5, the CF88 and Kunz models exhibit lower electron degeneracy in the core during this phase compared to the NACRE model.

At the end of core C burning (triangle in Fig. 3), the NACRE model exhibits a longer C-burning duration but lower $\xi_{2.5}$ compared to the CF88 model. This is due to the larger first C-burning convective shell in the NACRE model, which falls within the range used to evaluate compactness, thereby reducing the $\xi_{2.5}$. Additionally, the larger convective shell transports fresh ^{12}C into it, further prolonging the duration of this burning episode.

3.3 Advanced burning phases

Following the exhaustion of fuel in the first C-burning convective shell, the core contracts further, triggering Ne ignition at the center and forming a convective Ne-burning core (see also Fig. 4). The energy released from this process decelerates the advancing burning front, which eventually reaches the base of the second C-burning convective shell at the mass coordinates of $2.92 M_\odot$, $2.10 M_\odot$, and $1.75 M_\odot$ until the end of the evolution, for the NACRE, CF88, and Kunz models, respectively.

After the depletion of core Ne burning (cross in Fig. 3), the growth rate of $\xi_{2.5}$ differs significantly. For the NACRE model, $\xi_{2.5}$ increases significantly overall, because the mass coordinate at the base of the second C-burning convective shell is greater than the mass coordinate at which we evaluate the compactness. However, the evolution of $\xi_{2.5}$ displays two distinct peaks following the depletion of core O-burning (open circle in Fig. 3), with $\xi_{2.5}$ decreasing sharply after each peak. These oscillations in $\xi_{2.5}$ are primarily driven by the Si- and O-burning convective shells (Sukhbold & Woosley 2014; Renzo et al. 2017; Chieffi & Limongi 2020). The final $\xi_{2.5}$ is 0.44, corresponding to a final C-free core mass of $2.73 M_\odot$ (magenta dash-dotted line in Fig. 4), and the mass of the final iron core is $1.79 M_\odot$ (black dashed line in Fig. 4), which is constrained by the C-free core, determined by the location of the last carbon-burning shell (Brown et al. 2001; Schneider et al. 2021; Laplace et al. 2025). In contrast, for the CF88 and Kunz models, $\xi_{2.5}$ remains largely constant or decreases slightly, due to the mass coordinate at the base of the second C-burning convective shell being lower than the mass coordinate at which compactness is evaluated. Additionally, the oscillations in the subsequent evolution of $\xi_{2.5}$ are also driven by various convective shells. Ultimately, these two models form C-free cores with masses of $2.06 M_\odot$ and $1.75 M_\odot$, and corresponding iron cores with masses of $1.54 M_\odot$ and $1.46 M_\odot$, resulting in lower $\xi_{2.5}$ values of 0.16 and 0.08, respectively (see Table 1).

These results demonstrate how the $^{12}\text{C}(\alpha, \gamma)^{16}\text{O}$ reaction rate affects the pre-SN core structure. Our analysis identifies three distinct outcomes, as summarized in Table 1. The model using the NACRE rate exhibits the highest final compactness, $\xi_{2.5} = 0.44$, with $M_4 = 2.15$ and $\mu_4 = 0.13$. According to the

criteria of O'Connor & Ott (2011) and Ertl et al. (2016), this implies a likely failed explosion and BH formation, with the BH mass $M_{\text{rm,grav}} \approx 8.79 M_{\odot}$ computed using the semianalytic approach of Müller et al. (2016). However, for the models using the CF88 and Kunz rates, both criteria consistently predict a successful explosion, leading to the formation of a NS.

4 DISCUSSION

We investigated the effects of $^{12}\text{C}(\alpha, \gamma)^{16}\text{O}$ reaction rates on the evolution of a $14 M_{\odot}$ He stars and its pre-SN core structure, using three representative reaction rate combinations. As shown in Section 3, variations in the $^{12}\text{C}(\alpha, \gamma)^{16}\text{O}$ reaction rates significantly impact the pre-SN core structure, not only during the core He burning phase but also throughout the subsequent burning phases, particularly the C burning phase. In this phase, higher reaction rates reduce the available fuel for central C burning, leading to the transition from convective to radiative C burning, which is consistent with previous studies (e.g. Brown et al. 2001; Imbriani et al. 2001; Woosley et al. 2002; The et al. 2007; West et al. 2013; Sukhbold & Adams 2020; Patton & Sukhbold 2020).

Additionally, as shown in Fig. 4, the increase in the reaction rate extends the C-burning convective shells and shifts their locations, a result also observed in earlier studies (Brown et al. 2001; Imbriani et al. 2001; Woosley et al. 2002; El Eid et al. 2004; The et al. 2007). However, Pepper et al. (2022) found that higher reaction rates increase the core He burning lifetime in low- to intermediate-mass stars. In contrast, we found that reaction rates do not significantly affect the core He burning lifetime but significantly alter the lifetime of the core C burning phase. These differences in burning phases lead to variations in both the iron core mass and the core compactness parameter, which affect its explodability.

In this work, we considered the uncertainties of the $^{12}\text{C}(\alpha, \gamma)^{16}\text{O}$ reaction rate, while excluding the effects of uncertainties in the 3α , $^{12}\text{C} + ^{12}\text{C}$, and $^{12}\text{C} + ^{16}\text{O}$ reaction rates on the core structure. However, it is important to emphasize that the pre-SN core structure is also highly sensitive to these unconsidered key nuclear reactions, particularly during the advanced phases of evolution (Bennett et al. 2012; Pignatari et al. 2013; Fang et al. 2017; deBoer et al. 2017).

Among these reactions, although the 3α reaction rates are better constrained, even a 10% variation plays a significant role (Austin 2005). This is because the 3α reaction competes with the $^{12}\text{C}(\alpha, \gamma)^{16}\text{O}$ reaction in determining the ^{12}C abundance, which directly governs the conditions for C burning and ultimately affects both the core structure and the s-process yields (Tur et al. 2007, 2010). In addition, the $^{12}\text{C} + ^{12}\text{C}$ fusion reaction, the primary energy source during core C burning, significantly affects the core structure of the star. According to Bennett et al. (2012), an increased $^{12}\text{C} + ^{12}\text{C}$ reaction rate triggers earlier core C burning at lower temperatures, reducing neutrino losses and extending the burning lifetime. This uncertainty can also significantly affect the nature of core C burning (whether convective or radiative) and the number and locations of convective shell episodes. These changes ultimately impact both the pre-SN core structure and the final fate of stars (The et al. 2007; Bennett et al. 2012; Pignatari et al. 2013; Chieffi et al. 2021; Monpribat et al. 2022; Dumont et al. 2024). Furthermore, the $^{12}\text{C} + ^{16}\text{O}$ reaction rate can further contributes to energy generation during the merger of O- and C-burning shells, leading to a decrease in the core's compactness (Andrassy et al. 2020; Roberti et al. 2025; Laplace et al. 2025). The effect of the uncertainties in these

reactions is beyond the scope of this work. However, they may still affect the core structure and the final fate of massive stars. In the future, we will further investigate their effect on the pre-SN evolution and explosion mechanism, with a particular focus on explodability.

5 CONCLUSION

In this work, we investigated the impact of uncertainties in the $^{12}\text{C}(\alpha, \gamma)^{16}\text{O}$ reaction rate on the evolution of He stars, focusing on their pre-SN core structures by characterizing the iron core mass M_{Fe} and compactness parameter $\xi_{2.5}$. Our conclusions are as follows:

- We found that the $^{12}\text{C}(\alpha, \gamma)^{16}\text{O}$ reaction rate has varying degrees of effect on the M_{CO} and the $X_{\text{i}}(^{12}\text{C})$ at the end of core He burning, but significantly affects the subsequent core structure. Specifically, higher reaction rates lead to lower M_{CO} and $X_{\text{i}}(^{12}\text{C})$, resulting in the transition of central C burning from the convective to the radiative regime. This transition induces stronger neutrino losses, causing greater core contraction and a larger C-free core, which consequently leads to the formation of a larger iron core and a high value of compactness. These changes indicate a more compact pre-SN structure, which is harder to explode and is more likely to result in a BH remnant.
- We traced the evolution of compactness using different $^{12}\text{C}(\alpha, \gamma)^{16}\text{O}$ reaction rates and found that increasing this reaction rate significantly shifts the location of the last C-burning convective shell. When the location of the last C-burning convective shell exceeds the mass coordinate at which compactness is evaluated, the compactness increases significantly overall; otherwise, it remains essentially unchanged. Furthermore, the Si- and O-burning convective shells induce oscillations in compactness.
- A variation of the $^{12}\text{C}(\alpha, \gamma)^{16}\text{O}$ reaction rates affects the core C burning lifetime, with a lower reaction rate leading to a shorter lifetime. This triggers earlier central Ne ignition, which slows down the core contraction and prevents the C-burning front from advancing to higher mass coordinates. Ultimately, this leads to smaller iron core masses and lower final compactness.

Acknowledgements This study is supported by the National Natural Science Foundation of China (Nos 12288102, 12225304, 12090040/12090043, 12273105), the National Key R&D Program of China (No. 2021YFA1600404), the Youth Innovation Promotion Association of the Chinese Academy of Sciences (No. 2021058), the Yunnan Revitalization Talent Support Program (Yunling Scholar Project and Young Talent Project), the Yunnan Fundamental Research Project (No 202201BC070003, 202401AV070006, and 202201AW070011), and the International Centre of Supernovae, Yunnan Key Laboratory (No. 202302AN360001).

References

Aguilera-Dena, D. R., Langer, N., Antoniadis, J., et al. 2022, *A&A*, 661, A60 3
 Andrassy, R., Herwig, F., Woodward, P., & Ritter, C. 2020, *MNRAS*, 491, 972 9
 Angulo, C., Arnould, M., Rayet, M., et al. 1999, *Nucl. Phys. A*, 656, 3 3, 4
 Austin, S. M. 2005, *Nucl. Phys. A*, 758, 375 9
 Austin, S. M., West, C., & Heger, A. 2014, *Phys. Rev. Lett.*, 112, 111101 2
 Bennett, M. E., Hirschi, R., Pignatari, M., et al. 2012, *MNRAS*, 420, 3047 9

Böhm-Vitense, E. 1958, ZAp, 46, 108 3

Brown, G. E., Heger, A., Langer, N., et al. 2001, New Astron., 6, 457 3, 6, 8, 9

Buchmann, L. 1996, ApJ, 468, L127 2

Caughlan, G. R., & Fowler, W. A. 1988, Atomic Data and Nuclear Data Tables, 40, 283 3, 4

Chieffi, A., & Limongi, M. 2020, ApJ, 890, 43 2, 6, 7, 8

Chieffi, A., Roberti, L., Limongi, M., et al. 2021, ApJ, 916, 79 9

Costa, G., Bressan, A., Mapelli, M., et al. 2021, MNRAS, 501, 4514 2

Crowther, P. A. 2007, ARA&A, 45, 177 1

deBoer, R. J., Görres, J., Wiescher, M., et al. 2017, Reviews of Modern Physics, 89, 035007 2, 5, 9

Dessart, L., Yoon, S.-C., Aguilera-Dena, D. R., & Langer, N. 2020, A&A, 642, A106 1

Dumont, T., Monpribat, E., Courtin, S., et al. 2024, A&A, 688, A115 9

El Eid, M. F., Meyer, B. S., & The, L. S. 2004, ApJ, 611, 452 2, 9

Ertl, T., Janka, H. T., Woosley, S. E., Sukhbold, T., & Ugliano, M. 2016, ApJ, 818, 124 2, 3, 9

Ertl, T., Woosley, S. E., Sukhbold, T., & Janka, H. T. 2020, ApJ, 890, 51 1, 2, 3

Fang, X., Tan, W. P., Beard, M., et al. 2017, Phys. Rev. C, 96, 045804 9

Farmer, R., Laplace, E., Ma, J.-z., de Mink, S. E., & Justham, S. 2023, ApJ, 948, 111 2

Farmer, R., Renzo, M., de Mink, S. E., Fishbach, M., & Justham, S. 2020, ApJ, 902, L36 2

Farmer, R., Renzo, M., de Mink, S. E., Marchant, P., & Justham, S. 2019, ApJ, 887, 53 2

Herwig, F. 2000, A&A, 360, 952 3

Imbriani, G., Limongi, M., Gialanella, L., et al. 2001, ApJ, 558, 903 2, 9

Kunz, R., Fey, M., Jaeger, M., et al. 2002, ApJ, 567, 643 2, 3, 4

Langer, N. 2012, ARA&A, 50, 107 1

Laplace, E., Schneider, F. R. N., & Podsiadlowski, P. 2025, A&A, 695, A71 2, 3, 7, 8, 9

Monpribat, E., Martinet, S., Courtin, S., et al. 2022, A&A, 660, A47 9

Müller, B., Heger, A., Liptai, D., & Cameron, J. B. 2016, MNRAS, 460, 742 2, 3, 4, 9

O'Connor, E., & Ott, C. D. 2011, ApJ, 730, 70 2, 3, 9

Patton, R. A., & Sukhbold, T. 2020, MNRAS, 499, 2803 2, 3, 6, 7, 9

Paxton, B., Bildsten, L., Dotter, A., et al. 2011, ApJS, 192, 3 2

Paxton, B., Cantiello, M., Arras, P., et al. 2013, ApJS, 208, 4 2

Paxton, B., Marchant, P., Schwab, J., et al. 2015, ApJS, 220, 15 2

Paxton, B., Schwab, J., Bauer, E. B., et al. 2018, ApJS, 234, 34 2

Paxton, B., Smolec, R., Schwab, J., et al. 2019, ApJS, 243, 10 2

Pepper, B. T., Istrate, A. G., Romero, A. D., & Kepler, S. O. 2022, MNRAS, 513, 1499 9

Pignatari, M., Hirschi, R., Wiescher, M., et al. 2013, ApJ, 762, 31 9

Podsiadlowski, P., Joss, P. C., & Hsu, J. J. L. 1992, ApJ, 391, 246 1

Pols, O. R., & Dewi, J. D. M. 2002, PASA, 19, 233 1

Renzo, M., Ott, C. D., Shore, S. N., & de Mink, S. E. 2017, A&A, 603, A118 7, 8

Roberti, L., Pignatari, M., Brinkman, H. E., et al. 2025, A&A, 698, A216 9

Schneider, F. R. N., Podsiadlowski, P., & Laplace, E. 2023, ApJ, 950, L9 2

Schneider, F. R. N., Podsiadlowski, P., & Müller, B. 2021, A&A, 645, A5 2, 8

Sukhbold, T., & Adams, S. 2020, MNRAS, 492, 2578 2, 6, 7, 9

Sukhbold, T., Ertl, T., Woosley, S. E., Brown, J. M., & Janka, H. T. 2016, ApJ, 821, 38 2

Sukhbold, T., & Woosley, S. E. 2014, ApJ, 783, 10 2, 3, 6, 7, 8

The, L.-S., El Eid, M. F., & Meyer, B. S. 2007, ApJ, 655, 1058 9

Timmes, F. X., Woosley, S. E., & Weaver, T. A. 1996, ApJ, 457, 834 7

Tur, C., Heger, A., & Austin, S. M. 2007, ApJ, 671, 821 2, 9

Tur, C., Heger, A., & Austin, S. M. 2010, ApJ, 718, 357 2, 9

Ugliano, M., Janka, H.-T., Marek, A., & Arcones, A. 2012, ApJ, 757, 69 2

Weaver, T. A., & Woosley, S. E. 1993, Phys. Rep., 227, 65 2

West, C., Heger, A., & Austin, S. M. 2013, ApJ, 769, 2 2, 9

Woosley, S. E. 2019, ApJ, 878, 49 1

Woosley, S. E., & Heger, A. 2007, Phys. Rep., 442, 269 2

Woosley, S. E., & Heger, A. 2021, ApJ, 912, L31 2

Woosley, S. E., Heger, A., Rauscher, T., & Hoffman, R. D. 2003, Nucl. Phys. A, 718, 3 2

Woosley, S. E., Heger, A., & Weaver, T. A. 2002, Reviews of Modern Physics, 74, 1015 5, 9

Yoon, S.-C. 2017, MNRAS, 470, 3970 1, 3